AIAA JOURNAL
Vol. 59, No. 10, October 2021

Acoustical Holography-Based Analysis of Spatiospectral Lobes in High-Performance Aircraft Jet Noise

Kevin M. Leete*
Brigham Young University, Provo, Utah 84602
Alan T. Wall†
U.S. Air Force Research Laboratory, Wright–Patterson Air Force Base, Ohio 45433
Kent L. Gee‡ and Tracianne B. Neilsen§
Brigham Young University, Provo, Utah 84602
and
Michael M. James¶ and J. Micah Downing**
Blue Ridge Research and Consulting, Asheville, North Carolina 28801

https://doi.org/10.2514/1.J059400

Holographic reconstructions of the sound field in the vicinity of a tied-down F-35 aircraft were achieved by applying multisource statistically optimized near-field acoustical holography to measurements taken at a linear ground array approximately parallel to the shear layer of the jet. The measured field, as well as reconstructions to locations where the field was not measured, show that the field can be described as a superposition of multiple lobes in the spatiospectral domain. These lobes are observed in the field when the aircraft is operated at a variety of engine powers, including afterburner. For a given engine power, as frequency is increased, the spatial lobes in the mixing-noise region shift aft in directivity until they disappear beyond the aperture of the measurement while new ones appear toward the sideline and shift aft with the others. At a fixed frequency, when engine power is increased, the forward-most spatial lobe increases in level more than the other lobes, which is a major factor in the observed forward shift in overall directivity with increasing engine power. Frequency-dependent raytracing of the spatial lobes gives insight into the directivity and apparent source locations for jet noise components as a function of frequency and engine power.

Nomenclature

$\boldsymbol{A}$	=	hologram wave function matrix
c	=	speed of sound, m/s
dz	=	interelement spacing in z coordinate, m
H	=	Hermitian transpose operator
H_l^1	=	Hankel function of the first kind of order l
i	=	imaginary unit
k	=	acoustic wavenumber, m^{-1}
k_r	=	radial wavenumber, m^{-1}
k_z	=	axial wavenumber, m^{-1}
$\boldsymbol{p}$	=	complex pressure vector
$\boldsymbol{R}_{\boldsymbol{A}^{\mathrm{H}}\boldsymbol{A}}$	=	regularized inverse of $\boldsymbol{A}^{\mathrm{H}}\boldsymbol{A}$
$\boldsymbol{r}$	=	position vector
r, ϕ, z	=	cylindrical coordinates
r_0	=	reference radius, m
T	=	transpose operator
x, y, z	=	Cartesian coordinates, m
$\boldsymbol{\alpha}$	=	wave function matrix evaluated at reconstruction location
Δz	=	total span of array in z coordinate, m
ω	=	angular frequency, s^{-1}

Presented as Paper 2018-2826 at the 2018 AIAA/CEAS Aeroacoustics Conference, Atlanta, GA, June 25–29, 2018; received 8 January 2020; revision received 12 February 2021; accepted for publication 18 February 2021; published online 15 June 2021.

*Graduate Student, Department of Physics and Astronomy, N283 ESC. Student Member AIAA.
†Research Physicist, Battlespace Acoustics Branch, 2610 Seventh Street, Building 441. Member AIAA.
‡Professor of Physics, Department of Physics and Astronomy, N283 ESC. Senior Member AIAA.
§Associate Professor, Department of Physics and Astronomy, N283 ESC.
¶Chief Engineer, 29 North Market Street, Suite 700. Member AIAA.
**Chief Scientist, 29 North Market Street, Suite 700. Member AIAA.

I. Introduction

ALTHOUGH important insights are gained from laboratory-scale investigations of jet noise, some aspects of jet noise produced by full-scale military aircraft have not yet been reproduced by laboratory-scale measurements. Additional insight into aeroacoustic noise is, therefore, obtained by application of techniques used in laboratory settings to measurements of full-scale, high-performance military aircraft. Two such techniques are beamforming and near-field acoustical holography (NAH). Beamforming has been successfully used to image aeroacoustic sound sources in the laboratory [1,2] as well as at full scale [3–6]. Near-field acoustical holography, which was developed for the general three-dimensional imaging of noise fields [7,8], has been used in laboratory jet noise measurements [9–12] and was recently adapted to full-scale measurements of the jet noise produced by military aircraft [13,14]. The NAH process involves fitting an equivalent wave model (EWM) for the field under examination to measured data (called a hologram). This fitted EWM can then be evaluated at any point of interest and provides reliable estimations of the field as far as the assumptions in the EWM hold. Acoustical holography studies of jet noise from high-performance military aircraft have been successful in showing trends across frequency and engine conditions in both the source extent and directivity [14].

Wall et al. [15] used an advanced method of NAH called multisource statistically optimized NAH (M-SONAH) to investigate the characteristics of the field in the vicinity of an F-35 operating at 100% engine thrust request (ETR). Using a ground-based linear array as the input to the holography process, reconstructions were achieved over a large area within the aperture of the hologram. At several frequencies in the region of maximum radiation, multiple radiation lobes were observed. As frequency increased, as many as four individual lobes emerged toward the sideline, moved aft, and submerged back into the overall field. Evidence of broadband shock

associate noise (BBSAN) was also observed as a lobe propagating in the forward direction [16,17].

The presence of multiple radiation lobes in military aircraft jet noise has been seen in several data sets [18–21], although no conclusive explanation of its cause has been given. These lobes are described as either multiple peaks in the spectra at a given measurement location or as multiple local maxima in the directivity when plotting a single frequency across space. Evidence of spatiospectral lobe content in laboratory-scale measurements is sparse. In one example, Long [10] used NAH to image the source from a heated laboratory-scale jet and showed striation patterns in the spatial/spectral domain.

Several studies have proposed explanations for multiple lobes. Tam and Parrish [22] sought to explain dual spectral peaks shown in one-third octave band spectra of a rectangular-nozzled aircraft [23] in terms of indirect combustion noise sources that originate from within the nozzle. Liu et al. [24–27] investigated temperature ratio as a possible cause of multiple lobes by using large-eddy simulations of laboratory-scale jets and showed far-field evidence for at least two noise source mechanisms that became more distinct as temperature ratio was increased. Schmidt et al. [28], doing spectral proper orthogonal decomposition and resolvent analysis of large-eddy simulations of cold laboratory-scale jets, showed two main low-rank wavepacket structure types: one in the initial shear layer of the jet near the nozzle with a high phase speed and another downstream, more spatially extended and with a lower phase speed. These wavepacket types qualitatively agree with the two source mechanisms observed by Liu et al. [24–27], as discussed in Ref. [29].

Previous NAH [30] and beamforming [31] performed on measurements of military aircraft jet noise have constructed equivalent source models that have been successful in reproducing the sound field. These reduced-order equivalent source models use multiple independent sources to contribute to individual spatiospectral lobes, suggesting that the multiple lobes are incoherent. Swift et al. [32] performed extensive correlation and coherence analyses on the same data set presented in this paper that verify incoherence between lobes. The incoherence between the lobes suggests that they may be due to independent sources or source mechanisms. Additionally, Swift et al. [32] showed correlation between the aft radiation where multiple lobes are present and BBSAN in the forward direction, which suggests that shock cell interactions could be a contributor to these multilobe effects.

The purpose of the current study is to use M-SONAH, which was developed for the use of imaging the field produced in the presence of a ground reflection, to reconstruct the sound field produced by a tied-down F-35B aircraft running at various engine conditions. Trends in observed spatiospectral lobes and BBSAN across engine power are presented in a large area surrounding the jet for select frequencies. The measured and reconstructed fields show that the noise in the region of maximum radiation is a superposition of multiple spatiospectral lobes, where the overall trends across frequency and engine power are best described by the number and levels of the individual lobes present. Prior observations of a dual peak or multilobe phenomena by Wall et al. [14] and Tam et al. [20,22] appear to be subsets of the more complete picture described herein.

II. F-35 Measurement

This section discusses the measured spectra and overall sound pressure levels (OASPL) gathered from a ground-based array in the geometric near field approximately parallel to the jet shear layer and a far-field arc array 1.5 m off the ground. Spatiospectral lobes are seen at all engine powers.

A. Setup

Extensive static measurements of the F-35 A and B variants were performed at Edwards Air Force Base in 2013 [19]. The aircraft were tied down on a concrete run-up pad while the engine was cycled through various engine conditions, including 13 to 150% ETR. Engine powers greater than 100% ETR are due to the addition of afterburner. This paper uses measurements of the B variant, which had a Pratt & Whitney F135-PW-600 afterburning turbofan engine. The nozzle of the engine was 2 m from the ground and had a nominal 1 m diameter, although the exact nozzle diameter changed with engine condition. Jet parameters such as Mach number, nozzle pressure ratio, temperature, and exact nozzle diameter for each engine power are unknown by the authors, so no Strouhal number or other type of scaling is attempted in this work.

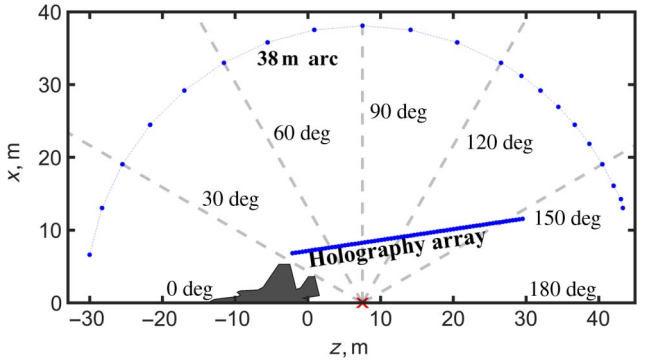

Fig. 1 Holography array and 38 m arc positions for the F-35B. The red marker is the microphone array reference point, which was 7.5 m behind the nozzle.

The coordinate system used in this study is centered on the nozzle exit (with the point on the ground below the nozzle exit as the origin), with the jet exhausting in the positive z direction, as illustrated in Fig. 1. The x axis is the horizontal distance from the jet centerline and the y axis is the height above the ground. Cylindrical coordinates are used in the M-SONAH algorithm, with r being the radial distance from the z axis. Another useful coordinate is the jet inlet angle θ, which is measured from the direction of the aircraft nose ($-z$ direction) around a microphone array reference point (MARP), which was located at $z = 7.5$ m. The array was laid out to the left side of the aircraft as shown in Ref. [19], although for ease of plotting and consistency with previous NAH studies, all plots here are mirrored to show it on the right side of the aircraft. This study focuses on a 32-m-long, 71-element (with 0.45 m interelement spacing) linear ground array placed approximately parallel to the shear layer, which is used as the input to the holography processing and is referred to as the holography array. An arc array located 38 m from the MARP is also used to validate the field reconstructions. Figure 1 shows a schematic for the test geometry with the coordinate system and the approximate location of the F-35B.

B. Measured Data

The measured data along the 71-microphone holography array demonstrate how the sound field varies with engine condition. The measured OASPL and corresponding spectra for each engine condition are shown in Figs. 2a and 3, respectively. As engine power

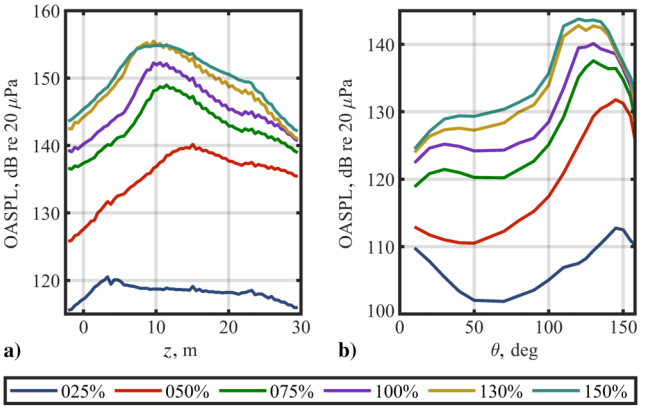

Fig. 2 OASPL across the a) holography array and b) 38 m arc for several F-35B engine conditions (given in % ETR).

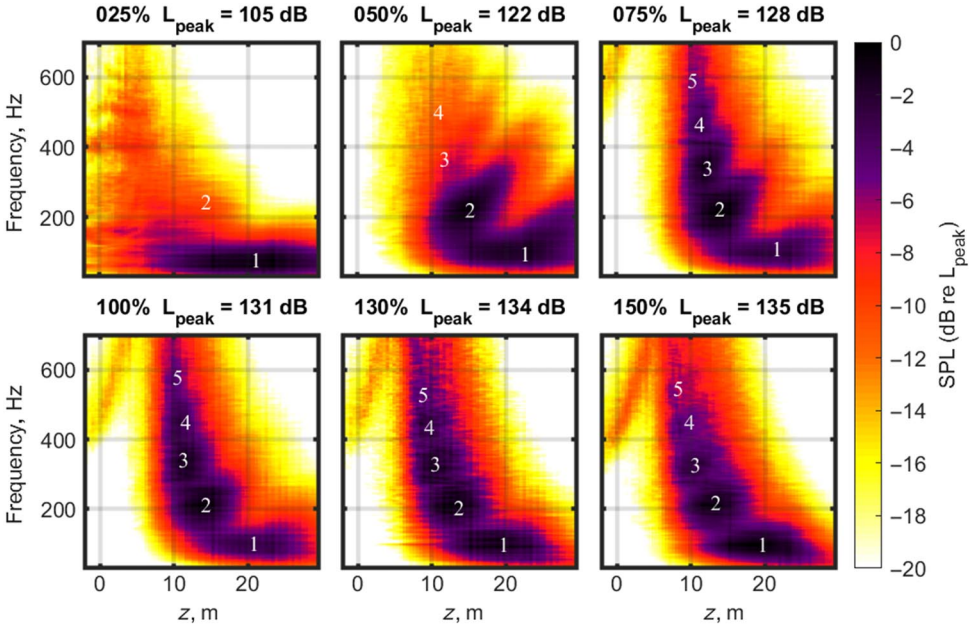

Fig. 3 Spatiospectral maps of normalized SPL on the holography array as a function of downstream distance from the nozzle and frequency. The numbers indicate the several spatiospectral lobes.

increases from 25 to 150% ETR, a peak in the OASPL appears at about $z = 15$ m at 50% ETR, shifts forward to about $z = 11$ m at 75%, and then continues shifting forward until it settles at about $z = 8$ m at 150% ETR. The transition between 130 and 150% ETR does not increase the OASPL significantly, except for rounding out the peak. At 50% ETR and above, a secondary local maximum is seen at about $z = 22$ m. The far-field OASPL measured at the 38 m arc in Fig. 2b shows the forward shift in directivity as engine power is increased, although both afterburning conditions have similar curves. The increased level in the forward direction at 25% ETR is attributed to aircraft noise, but at 75% ETR and above, the increase in the forward directions is due to BBSAN [16]. There are hints of a split directivity in the OASPL at 75% ETR and greater, although the deviation is too small and the angular spacing of the array is too large to be sure. The OASPL directivity shifts from being centered at approximately 145 deg at 25% ETR to 125 deg at afterburner.

The spectra at each point on the holography array illuminate why the OASPL changes as it does. Figure 3 shows the sound pressure levels (SPLs) for frequencies between 30 and 700 Hz (spacing of 3 Hz) for each microphone along the array. Each pane of Fig. 3 shows the data for an engine condition (specified above the pane). The color bar on the right (shared across panes) shows the levels relative to the peak, which is specified above each pane. At 25% ETR, the left portion of the array ($z < 10$ m) appears to be dominated by engine noise, with the louder jet noise farther aft. At 50% ETR and above, jet noise dominates the whole array. For engine conditions at 75% ETR and above, radiation in the forward direction is observed between 300 and 700 Hz, which analyses in Refs. [16,17] show to be BBSAN.

The most prominent feature of the spatiospectral plots in Fig. 3 is the presence of multiple lobes in the space-frequency domain. There are at least two lobes at 25% ETR, four lobes between 50 and 130% ETR, and five at 150% ETR. Deciphering the exact number of lobes is an ongoing research problem, with different methods being employed. For this work, the patterns of minima and maxima in the levels are used, as indicated by the white numbers on the spectra in Fig. 3.

The placement of each lobe in the spatiospectral domain appears consistent across engine conditions, although their individual extent, shape, and relative amplitudes differ greatly. A clear example is the difference between the 50 and 75% ETR engine conditions; lobe 4 is barely visible in the 50% ETR case, but in the 75% ETR case, it has a much greater contribution to the field. The significant addition of upstream energy in the third and fourth lobes in the transition from 50 to 75% ETR appears to be the single greatest contributor to the increase in OASPL and the forward shift in directivity seen in Fig. 2. Qualitatively, the total spectrum appears to be a simple superposition of these lobe structures, which would imply an incoherence between them. These observations seem to show that the aft radiation region, which has been attributed to large-scale turbulent structure noise may actually be a superposition of different noise mechanisms. Analyses in Secs. IV.D and IV.D.2 of this paper are geared to understand the source regions in the jet plume responsible for these spatiospectral lobes, although additional work is needed to understand if these are universal aeroacoustic phenomena or only apply to military aircraft jet noise.

III. M-SONAH Method

This section discusses the application of M-SONAH to the F-35B measurements (described in Sec. II) to reconstruct the time-averaged complex pressure field in the area surrounding the aircraft. M-SONAH, developed by Wall et al. [13], modifies the traditional SONAH algorithm [33] to use a two-source model: one along the jet centerline and an image source, equidistant from but below the ground, to account for the ground reflection. Each source has a corresponding set of cylindrical basis functions that constitute the EWM of the field. The time waveforms recorded from the holography array are the input to the M-SONAH algorithm, which includes the following steps.

A. Extract Frequency-Dependent Complex Pressures from Recorded Pressure Waveforms

To obtain the frequency-dependent complex pressures for all measurement locations and engine conditions, the recorded 30 s time waveforms are split into multiple blocks with a 50% overlap and windowed with a Hann function. The Fourier transform is then applied to each block. During the F-35B measurements, several organizations and different data acquisition systems with different sampling frequencies were involved in the simultaneous measurement of all the microphone channels. For this study, the block sizes for each different sampling rate were chosen such that the resultant frequency resolution was 3 Hz in all cases. The applied Fourier transform yields a single complex pressure value per block, per frequency. The remaining steps are done on a frequency-by-frequency basis.

B. Perform a Partial Field Decomposition to Generate Mutually Incoherent Partial Fields

Application of acoustical holography fundamentally assumes that the field in question is coherent. Therefore, to apply NAH to partially

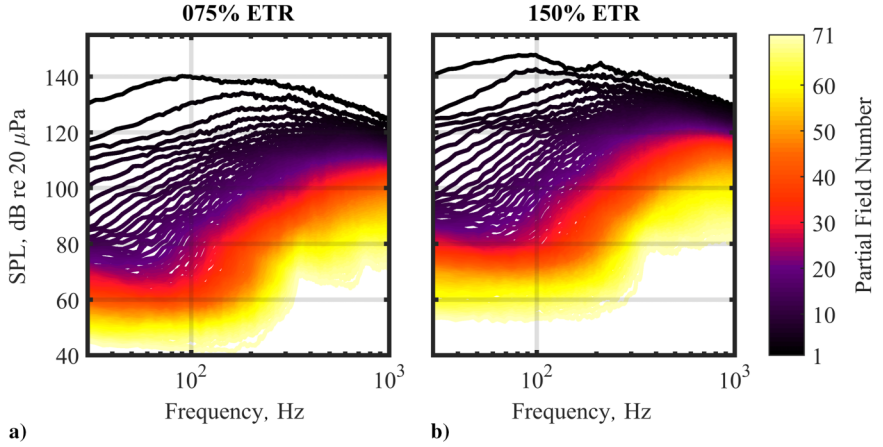

Fig. 4 Singular values of the 71 partial fields as a function of frequency for a) 75% and b) 150% ETR.

coherent jet noise, the complex pressures on the holography array are decomposed into mutually incoherent but self-coherent partial fields that can be processed independently. After propagation, the individual partial fields are summed energetically to reproduce the total field [34]. For each frequency, the cross-spectral matrix (CSM) of the input array is calculated. The CSM is a matrix where the ijth entry is the cross spectrum between elements i and j in the array. A singular value decomposition (SVD) is done on the CSM, where the singular vectors of the SVD scaled by their corresponding singular values yields a set of partial fields. The number of partial fields generated is equal to the number of elements in the input array. Figure 4 shows the SPLs of the singular values for two representative engine powers. These singular values indicate the contribution of each partial field at each frequency. At low frequency, the field exhibits low-rank behavior; the majority of the energy is compacted by the SVD into relatively few partial fields.

Since each partial field is processed individually and the final reconstructed field is a sum of all the processed partial fields, a filtering of sorts can be done by only using the most energetic partial fields to reconstruct the total field. In this study, for each frequency of interest, the number of partial fields used was selected such that their sum represented 99.9% of the total energy of the input hologram. Over the frequency band presented in this paper, only four partial fields were needed to meet this energy criteria for the lowest frequencies and on the order of 50 for the highest frequencies. Because the excluded partial fields generally had higher relative amplitudes toward the edges of the array, the 0.1% of energy removed generally causes the field at the edges of the array to be slightly underestimated.

C. Numerically Extrapolate Each Partial Field Beyond the Measurement Aperture

The SONAH algorithm was originally developed to reduce errors caused by having a measurement aperture that was not significantly larger than the source [33]. Even with the SONAH algorithm, in this measurement, the 32 m aperture was not large enough to capture all the pertinent energy for the lowest frequencies, causing finite-aperture effects to become significant. The two most significant finite-aperture effects in this work are wraparound error and high-wavenumber leakage. Wraparound error is solved easily by zero-padding the edges of the input hologram so that it is much larger than the area in which the reconstructions are made. Leakage of high wave numbers is caused by pressure discontinuities in the input, which in turn are caused by the pressures not decaying to zero by the edges of the hologram. In an attempt to simulate the missing energy from having a too-small aperture at low frequencies and to reduce the discontinuity at the measurement edge, linear forward prediction was implemented to estimate values for the complex pressures of the field at locations beyond the original measurement aperture and a window was applied to the extended measurement to reduce the pressures to zero by the edge.

In linear forward prediction, the coefficients of a polynomial are determined from existing data, and the polynomial is used to predict one point beyond the original aperture, which is then included in the fitting of a new polynomial. This process is iterated until the field is extended the desired amount. This method has been used for previous studies [35] and is repeated here for simplicity. A challenge with extending the aperture of each partial field individually is that the SVD-based partial field decomposition may generate partial fields that do not monotonically decrease toward the end of the original measurement. In such cases, the linear forward prediction (which has a tendency to produce extraneous oscillations [35]) of the higher-order partial fields (which via the SVD are inherently less energetic than the lower-order partial fields) often end up contributing more to the energy of the extended field than the lower-order partial fields. This causes the extended field to only be accurate for short distances outside of the original measurement. To enforce a graceful taper of the pressures to zero at the end of the extended aperture and reduce the effect of extraneous oscillations outside the original measurement, a Tukey window is applied to the magnitude of the complex pressures along the extended hologram. The window has a value of one over the original measurement that decays to a value of zero within one acoustic wavelength of the edge of the original measurement. Extending the aperture with the window provides zero-padding as well. For this measurement geometry, the aperture is extended approximately 68 m on either side of the array, which is needed to eliminate wraparound error for as low as 32 Hz.

D. Formulate the Equivalent Wave Model of the Jet in the Run-Up Pad Environment and Solve for Pressure at Desired Reconstruction Locations

The EWM methodology used in the M-SONAH algorithm is described in detail in Refs. [13,14]. For this study, the EWM is comprised of two sets of cylindrical wave functions to capture the effect of the rigid ground on the measurement, one centered along the jet centerline and another along an image jet centerline below the ground. The basis functions for outward propagation are

$$\Psi_{l,k_z}(\boldsymbol{r}) \equiv \frac{H_l^1(k_r r)}{H_l^1(k_r r_0)} e^{il\phi} e^{ik_z z}, \qquad r \geq r_0 \tag{1}$$

where r, ϕ, and z are the radial, azimuthal, and axial spatial coordinates of the position vector $\boldsymbol{r}$; H_l^1 is the lth-order Hankel function of the first kind; i is the imaginary unit; r_0 is some small reference radius (traditionally the assumed source radius) [36]; and k_z and k_r are the axial and radial wave numbers, respectively. For this study, only $l = 0$ is used, since a single, ground-based linear array is used as the input. This choice of l forces axisymmetry for each wave function at each frequency. This limitation is sufficient to reconstruct the sound field over a limited azimuthal aperture, as exemplified by the success of prior work [14], where a large two-dimensional array was used as input but only the zeroth-order mode was needed for accurate

reconstructions. The success of limiting the equivalent wave model to $l = 0$ is likely due to the reconstructions only being attempted at sufficiently low frequencies.

The number of wave functions in each set M is therefore only dependent on the number of k_z values used. The k_z values for this study are regularly spaced between $-\pi/dz$ and π/dz in steps of $\pi/\Delta z$, where dz is the interelement spacing along the array in z and Δz is the total axial span of the array. The radial wave numbers are

$$k_r = \begin{cases} \sqrt{k^2 - k_z^2} & \text{for } |k| \geq |k_z| \\ i\sqrt{k_z^2 - k^2} & \text{for } |k| < |k_z| \end{cases} \tag{2}$$

where $k = \omega/c$ is the acoustic wave number, ω is the angular frequency, and c is the speed of sound. This choice for wave function and definition of k implies a time harmonicity of $e^{-i\omega t}$.

The basis functions in Eq. (1) depend on a position vector $\boldsymbol{r} = (r, \phi, z)$, which is expressed relative to the above-ground jet centerline (superscript [1]) or the image jet centerline below the ground (superscript [2]) via Eqs. (3) and (4):

$$\boldsymbol{r}^1 = \left(\sqrt{x^2 + (y-2)^2}, \tan^{-1}\left(\frac{y-2}{x}\right), z\right) \tag{3}$$

$$\boldsymbol{r}^2 = \left(\sqrt{x^2 + (y+2)^2}, \tan^{-1}\left(\frac{y+2}{x}\right), z\right) \tag{4}$$

using the Cartesian coordinates of Fig. 1. The notation $\boldsymbol{r}_{h_i}$ is now used to represent the position vector of the ith point on the holography array (which has N_h points), and $\boldsymbol{r}_{q_i}$ represents the position vector of the ith of N_q points on the reconstruction array.

The total EWM is now created by evaluating all the basis functions at each measurement point and each reconstruction point. They are combined into the matrices

$$\boldsymbol{A} = \begin{pmatrix} \Psi_{k_{z1}}(\boldsymbol{r}^1_{h1}) & \cdots & \Psi_{k_{z1}}(\boldsymbol{r}^1_{hN_h}) \\ \vdots & \ddots & \vdots \\ \Psi_{k_{zM}}(\boldsymbol{r}^1_{h1}) & \cdots & \Psi_{k_{zM}}(\boldsymbol{r}^1_{hN_h}) \\ \Psi_{k_{z1}}(\boldsymbol{r}^2_{h1}) & \cdots & \Psi_{k_{z1}}(\boldsymbol{r}^2_{hN_h}) \\ \vdots & \ddots & \vdots \\ \Psi_{k_{zM}}(\boldsymbol{r}^2_{h1}) & \cdots & \Psi_{k_{zM}}(\boldsymbol{r}^2_{hN_h}) \end{pmatrix} \tag{5}$$

and

$$\alpha = \begin{pmatrix} \Psi_{k_{z1}}(\boldsymbol{r}^1_{q1}) & \cdots & \Psi_{k_{z1}}(\boldsymbol{r}^1_{qN_q}) \\ \vdots & \ddots & \vdots \\ \Psi_{k_{zM}}(\boldsymbol{r}^1_{q1}) & \cdots & \Psi_{k_{zM}}(\boldsymbol{r}^1_{qN_q}) \\ \Psi_{k_{z1}}(\boldsymbol{r}^2_{q1}) & \cdots & \Psi_{k_{z1}}(\boldsymbol{r}^2_{qN_q}) \\ \vdots & \ddots & \vdots \\ \Psi_{k_{zM}}(\boldsymbol{r}^2_{q1}) & \cdots & \Psi_{k_{zM}}(\boldsymbol{r}^2_{qN_q}) \end{pmatrix} \tag{6}$$

where the number of rows in $\boldsymbol{A}$ is equal to the number of wave functions used in the model (twice the M discrete k_z values), and the number of rows is equal to the N_h measurement points on the hologram. The α martrix has the same number of rows as $\boldsymbol{A}$, but with columns equal to the N_q number of points in the array where the field is to be reconstructed.

At this point, the M-SONAH process is the same as SONAH [33], where the column vector of pressures at all the reconstruction locations $\boldsymbol{p}_q$ is given in terms of the column vector of pressures at each point of the hologram $\boldsymbol{p}_h$ as

$$\boldsymbol{p}_q^{\mathrm{T}} = \boldsymbol{p}_h^{\mathrm{T}} \boldsymbol{R}_{\boldsymbol{A}^{\mathrm{H}}\boldsymbol{A}} \boldsymbol{A}^{\mathrm{H}} \alpha \tag{7}$$

where the superscript T is the transpose, the superscript H is the Hermitian transpose, and $\boldsymbol{R}_{\boldsymbol{A}^{\mathrm{H}}\boldsymbol{A}}$ is the regularized inverse of $\boldsymbol{A}^{\mathrm{H}}\boldsymbol{A}$. Regularization was performed using a modified Tikhonov filter with the generalized cross-validation procedure for the selection of the regularization parameter as outlined in Ref. [37]. The reconstructed pressures for each partial field are then energetically summed to obtain the final answer for each frequency. All levels shown in this paper for specific frequencies are scaled as if these frequencies were extracted from an autospectrum with units of Pa^2.

IV. Results and Discussion

This section shows the reconstructed field in the area surrounding the aircraft. In Sec. IV.A, the field is reconstructed along the holography array to verify the spatial and frequency regions where reliable reconstructions are obtained. Section IV.B contains reconstructions to the two-dimensional plane along the ground surrounding the aircraft as well as comparisons of reconstructions to the measured field along the 38 m arc. Section IV.C has the reconstructions that were made along the nozzle lipline of the jet to give insight into acoustic source characteristics of the jet plume. Section IV.D.1 shows reconstructions made to the field in the region to the side of the aircraft to characterize BBSAN directivity and source location. In Sec. IV.D.2, the region of maximum radiation in the aft direction is examined and the field sound level maps are used to characterize the behavior of the multiple spatiospectral lobes across frequency and engine power. Finally, Sec. IV.E compares these results to previous studies of similar military aircraft as well as a numerical simulation of a heated laboratory-scale jet.

A. Reconstructions at the Hologram

To verify the frequency range in which the aperture and interelement spacing of the array are sufficient, field reconstructions are made at the input array and compared to the measured data. The differences between the reconstructed and measured fields are displayed in Fig. 5 for two engine conditions: an intermediate condition (75% ETR) and the maximum afterburning condition (150% ETR). The largest errors in the reconstruction occur at low frequencies, where the method overestimates the field level, and at high frequencies (above 400 Hz), where the levels are underestimated. The low-frequency errors are attributed to the array not being large enough to fully capture all the pertinent energy in the field. The high-frequency underestimations are due to spatial aliasing, where the trace wavelength of the noise along the array is smaller than twice the interelement spacing in the array. The spatial aliasing at frequencies above 400 Hz causes a reallocation of energy to a nonphysical lobe that starts far downstream and propagates upstream. This reallocation of energy is manifest as an immediate drop in level at about 400 Hz for $z > 10$ m. The upstream region ($z < 10$ m, where BBSAN is dominant) maintains a smaller error for frequencies above 400 Hz until the aliased lobe causes an overestimation of the levels there (particularly at 75% ETR). Based on these limitations, investigations into the directivity of the aft radiation lobes are only conducted for frequencies less than 400 Hz.

B. Field Reconstructions

The benefit of the holography process is its ability to reconstruct the field at arbitrary locations, which gives a physics-based extrapolation of the field to a myriad of points that would be impractical to measure. Figure 6 shows reconstructions of the field to points in the ground plane ($y = 0$) for two representative frequencies and engine conditions. The top row corresponds to 162 Hz and the bottom row to 354 Hz. The columns represent two engine conditions: on the left, an intermediate condition (75% ETR) and on the right, the maximum afterburning condition (150% ETR). The color contour maps show the reconstructed sound pressure level (SPL) at each point, the white line is the holography array location, and the gray outline is the aircraft position. In general, the reconstructions show field trends

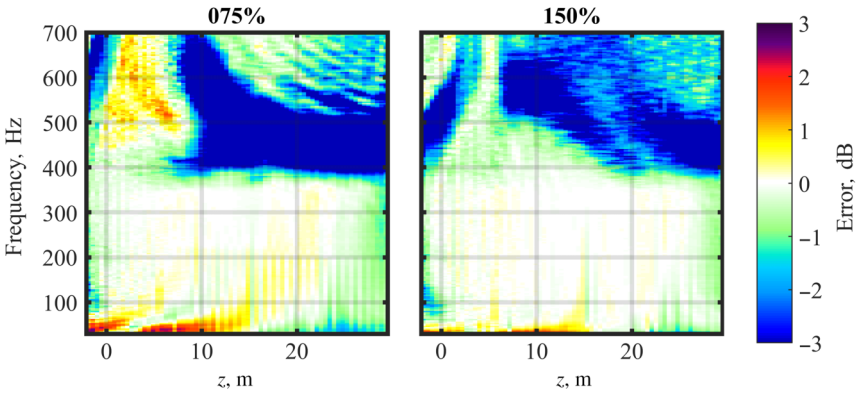

Fig. 5 Error of the M-SONAH reconstruction along the input holography array as a function of frequency for two engine conditions, 75% and 150% ETR.

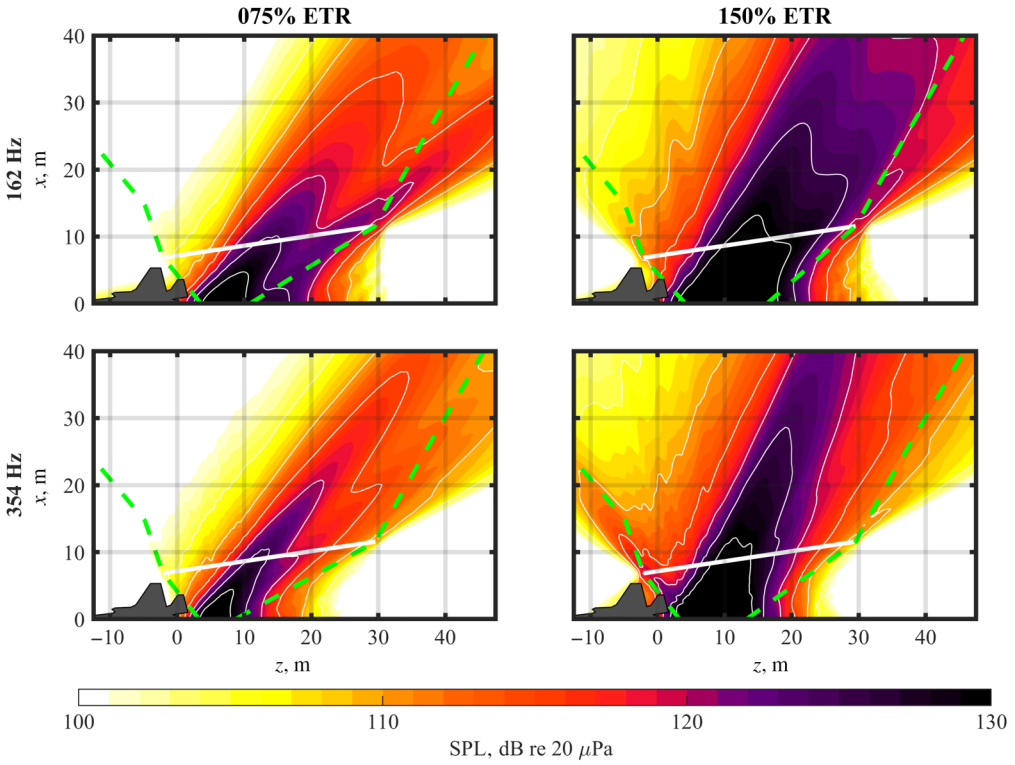

Fig. 6 Reconstructions along the $y = 0$ plane at two frequencies and engine conditions.

expected for jet noise, with the maximum radiation beaming at a large aft angle. However, the most apparent features at these frequencies are the multiple radiation lobes. At 75% ETR and 162 Hz, two lobes are present with distinct directivities and apparent source locations; at the same frequency but 150% ETR, the lobes rotate to a more forward directivity, have a higher level, and overlap more. The same trend (although less clear) can be seen at 354 Hz.

To be able to characterize the directivity of the multiple lobes across frequency and engine power, it is important to understand the spatial limitation of accurate field reconstructions. Although not shown in Fig. 1, the F-35 measurement contained a number of arrays in the field, including arcs with radii of 19, 29, 38, and 76 m as well as additional line arrays in front of and just behind the holography array. A previous study [38] compared M-SONAH reconstructions to the measurements at these arrays and found errors were less than 2 dB between $\theta = 50$ and 150 deg. Further investigation of the artifacts of the M-SONAH procedure was done using a numerical simulation. A numerical source was created along the jet centerline, the M-SONAH procedure was applied to an input hologram (same spatial location as the F-35 measurements), and field reconstructions of the numerical source were compared to the numerical field. The 2 dB error contours of this numerical case are used in conjunction with the error of the M-SONAH reconstructions to all the measurements in the region to determine a conservative estimate of a region of good fit for the frequencies of interest in this paper. The boundary of the good-fit region is represented by the dashed green lines in Fig. 6. A line is drawn from the edges of the holography array outward to select microphone positions at the 19, 38, and 76 m arcs. Upstream of the main radiation lobe, the boundary points are chosen as $\theta = 50$ deg for the 19, 38, and 76 m arcs and, downstream of the main radiation lobe, $\theta = 140$ deg for the 38 m arc and $\theta = 130$ deg for the 76 m arc. These lines are continued from the edges of the holography array inward to the nozzle lipline to the spatial region that contains the top 6 dB of reconstructed levels at each frequency (discussed further in Sec. IV.C).

The accuracy of the outward reconstructions is confirmed by comparing reconstructions to measured spectra along the 38 m arc. Figure 7 shows five spectra measured at 110, 120, 130, 140, and 150 deg at two engine conditions, along with the M-SONAH reconstructions at the corresponding measurement locations (dotted lines).

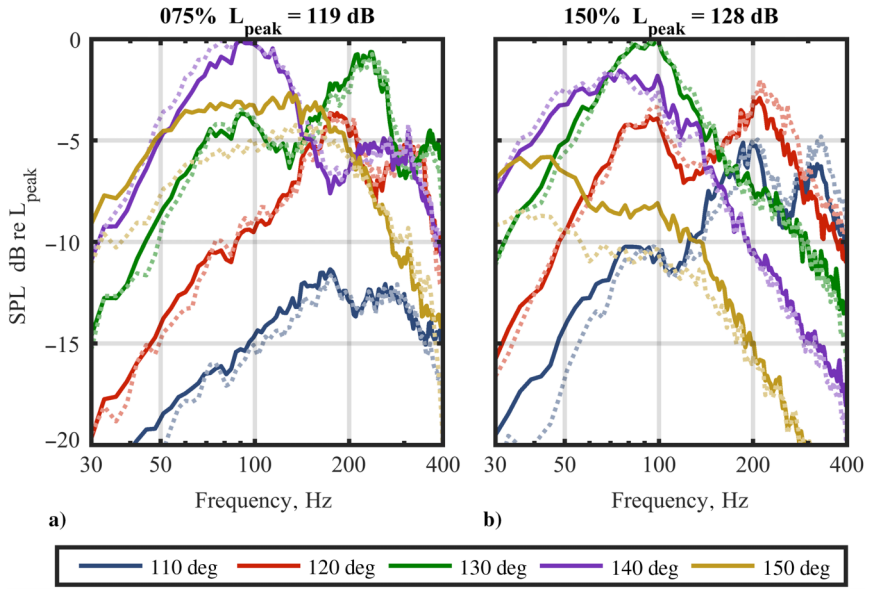

Fig. 7 Select spectra along the 38 m arc at five polar angles and two engine conditions. Dotted lines are M-SONAH reconstructions.

The spectra are limited between 30 and 400 Hz and normalized to the peak of the spatiospectral domain (similar to Fig. 3). Although the measurement was taken at 5 ft off the ground, the multipeaked spectra observed at all engine conditions are not attributed to ground reflection interference nulls. Because of the large distance of the array from the jet, the lowest frequency where ground reflection nulls for even an infinitely long cylindrical source at the jet centerline is calculated to be above 400 Hz. Reconstructions follow the measured spectra closely except for frequencies below 150 Hz at the 150 deg location, where the reconstructions underestimate the levels, likely due to the limitations in the aperture extension procedure.

To provide a more complete view of the aft radiation, holographic reconstructions to a dense grid along the 38 m arc are shown in Fig. 8 in the same format as Fig. 3, with the exception that the horizontal axis is now the jet inlet angle θ. The M-SONAH reconstructions appear to interpolate between the measured spectra in Fig. 7 and show up to three clearly defined spatiospectral lobes in this frequency range.

C. Source Reconstructions

M-SONAH reconstructions at the nozzle lipline for the F-35B (along the line at $x = 0.5$ m, $y = 2.0$ m) can provide insight into source characteristics. Spatiospectral reconstructions to the nozzle lipline are displayed in Fig. 9, which is in the same format as Fig. 3. Each pane represents the reconstructions between 30 and 700 Hz at each point along the lipline. The green contour lines represent the spatial region where the levels are within 6 dB of the maxima at that frequency. For a given engine condition, the peak region of the source contracts in size and shifts upstream with frequency, which is well-documented for subsonic [39] and supersonic [40,41] jet noise at laboratory scales. However, like previous studies of tactical aircraft [6,14], there are some deviations in the source distributions. At 25% ETR between 200 and 400 Hz, there seem to be two spatially separated local maxima. The upstream maximum is possibly an attempt by the algorithm to reconstruct the engine noise, while the other is the reconstruction of the aeroacoustic noise, with lower frequencies dominated by aeroacoustic noise and higher frequencies

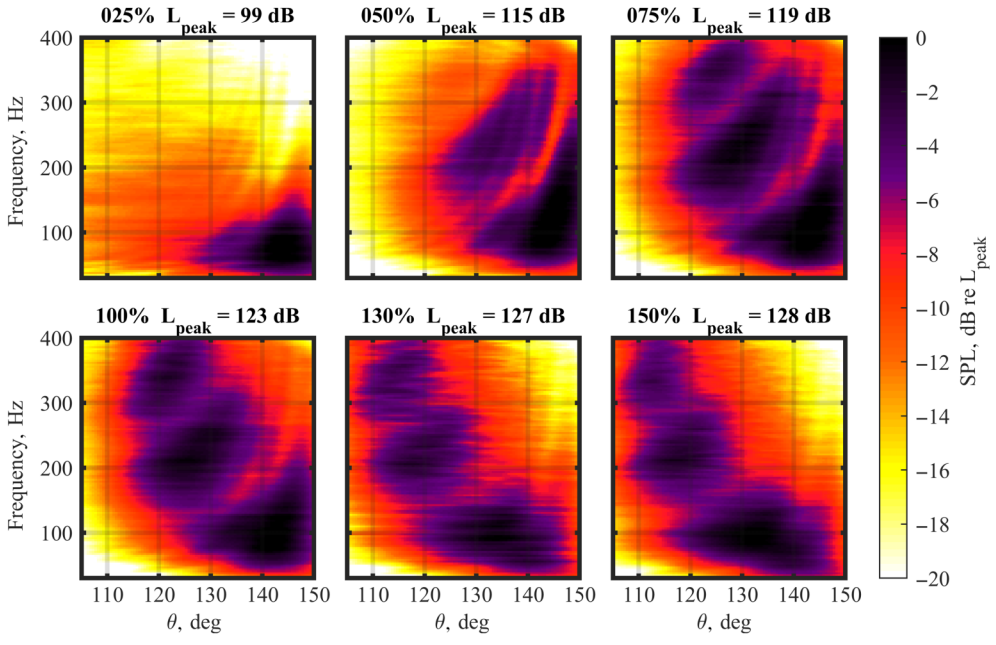

Fig. 8 Reconstructed spatiospectral maps along the 38 m arc in the same format as Fig. 3.

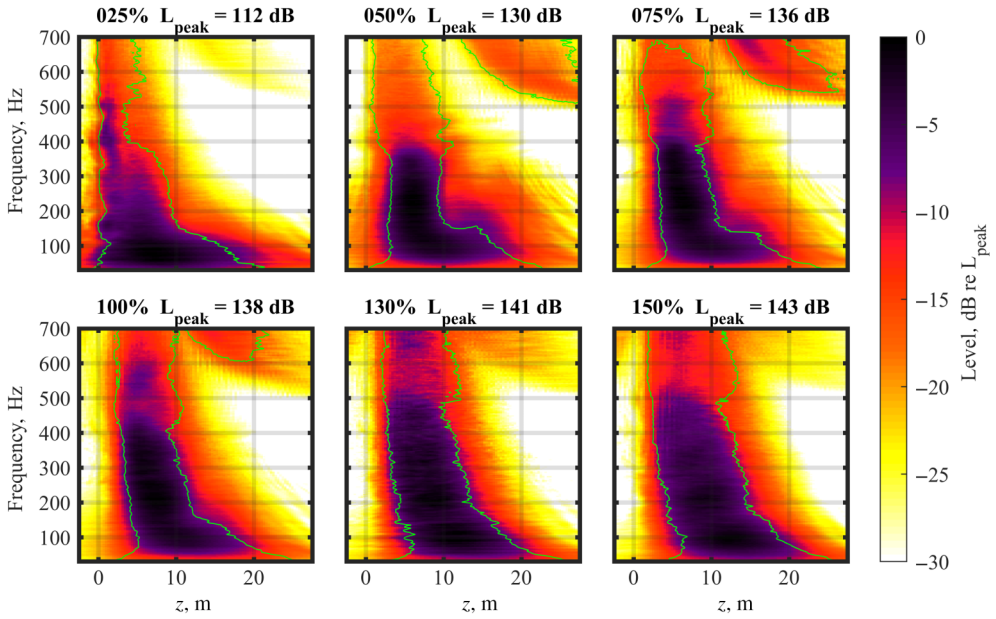

Fig. 9 Spatiospectral maps of M-SONAH reconstructions along the nozzle lipline.

dominated by engine noise. Spatiospectral lobes are seen at 50% ETR and above that follow similar patterns as in Fig. 3. At 50 and 75% ETR though, instead of discrete lobes as seen in Fig. 3, it appears as more of a continuous L-shaped region. At 130 and 150% ETR, however, the spatiospectral levels in Fig. 9 start to mimic the measured data at the input array and split into separate lobes similar to those in Fig. 3.

As previously mentioned, spatial aliasing starts to appear in the field reconstructions at 400 Hz. Even though an aliased lobe does not appear at the lipline until above 500 Hz, at 50, 75, and 100% ETR, there is an enlargement of the marked 6 dB down region between 400 and 500 Hz. The enlargement is probably due to the spatial aliasing, as it does not follow trends measured from similar full-scale military aircraft [6].

D. Multiple Lobe Tracing

The multiple radiation lobes can now be tracked across space because of the holographic projection of the field between measurement arrays. First, the field was reconstructed to a dense polar grid (with the MARP as the origin) along the ground plane in the vicinity of the aircraft. This projection onto the ground plane provides an approximation of the lobes that would be found in a free-field analysis (lobe tracing at the jet centerline height with no ground interference effects). Examples of these field reconstructions are seen in Fig. 6. To capture trends of the multiple spatiospectral lobes across frequency and engine power, lines were fit in the z–x plane to each of the spatial lobes at each frequency, similar to laboratory-scale work where the field could be measured directly [42]. To trace the lobes, points of local maxima were selected along each radius of the dense polar grid programmatically. Several local maxima were seen at each arc due to the multiple radiation lobes in the aft direction, the BBSAN noise lobe in the forward direction, and noise in the reconstruction. To identify which points correspond to spatiospectral lobes, these points were then overlaid over plots of the complete field reconstructions such as in Fig. 6 to see them in context. Each plot for every frequency and engine power combination was then viewed to manually select which points were representative of each directivity lobe in the field. Lines in the z–x plane were then least-squares fit to each group of selected points to create a line to represent each directivity lobe. This resulted in a set of lines that represent specific directivity lobes at individual frequencies.

The lines with a positive slope (representing a spatial lobe with aft directivity) for each frequency were then associated with each of the spatiospectral lobes as numbered in Fig. 3. This association was done by calculating the intersection point of each line with the holography array and superimposing those points on Fig. 3. Each point (representing a traced line at a single frequency) was then manually assigned to one of the numbered spatiospectral lobes. This process contains some ambiguity in that sometimes more than one spatial local maximum at a single frequency appears to be a part of a single spatiospectral lobe as numbered in this paper. This suggests that the spatiospectral lobes as numbered in Fig. 3 are in fact not capturing all the physical phenomena present. However, for the purposes of this paper, these smaller fluctuations are ignored. Further analyses to quantitatively isolate finer patterns than the several lobes discussed in this paper (such as coherence analyses [32]) are ongoing.

The slope and z intercept of each line now give information about the directivity and apparent source location of each spatiospectral lobe and can be tracked as a function of frequency and engine power. This procedure for tracking the spatiospectral lobes is used in Secs. IV.D.1 and IV.D.2 to discuss the trends of the BBSAN lobe in the upstream direction and the multiple radiation lobes in the aft direction.

1. *BBSAN Trends*

BBSAN has been explored in much more detail in the jet noise literature than the spatiospectral lobes radiating in the aft direction. The characteristic spatiospectral signature can be seen along the holography array (Fig. 3) for 75, 100, 130, and 150% ETR between 400 and 700 Hz at $z < 7$ m. M-SONAH reconstructions of the field show BBSAN as a lobe radiating upstream. Figure 10 shows M-SONAH reconstructions along the ground plane at two representative frequencies from 75 to 150% ETR. At 450 Hz, there is little evidence of BBSAN at 75% ETR, but it quickly strengthens as engine condition increases. At 549 Hz, BBSAN is apparent at 75% ETR and increases in strength up to 150% ETR. The lines fitted to the BBSAN lobes are superimposed on Fig. 10 in dark blue.

The reconstructions at frequencies above 400 Hz (as shown in Fig. 10) are considerably noisier than the low-frequency reconstructions seen in Fig. 6. This noise arises during the regularization step in the inversion of $\boldsymbol{A}^{\mathrm{H}}\boldsymbol{A}$, which becomes more difficult as frequency increases (particularly above the Nyquist frequency when aliasing is present). A more stringent choice of regularization parameter significantly smooths out the field but also causes the level to be severely underestimated. The parameter used here was chosen to favor accuracy in level.

To track the BBSAN lobe characteristics across frequency and engine condition, Fig. 11 shows the directivity angle and z intercept

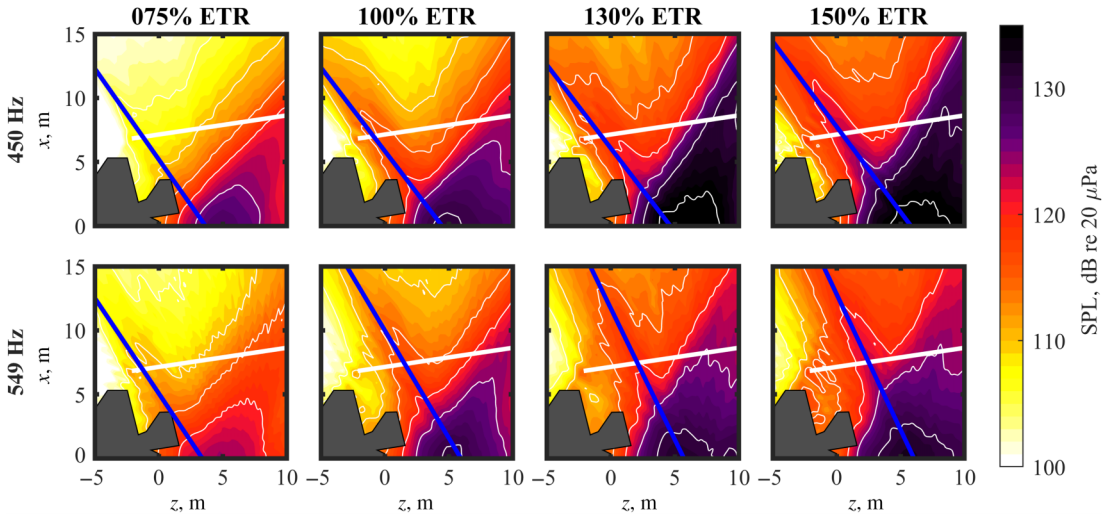

Fig. 10 Reconstructions along the ground plane of the region toward the side of the aircraft where BBSAN is apparent.

of lines fitted to the BBSAN lobe for several engine conditions. Little variation across engine condition is seen, except for the z intercept at 75% ETR. The BBSAN at this engine power is low in level and appears at the edge of the holography array, as seen in Figs. 3 and 10. The low prominence of the BBSAN lobe and incomplete coverage by the array likely causes the fitted line to be less accurate than at higher engine powers, where the BBSAN lobe is fully captured. For all engine conditions, however, the placement of the origin of BBSAN in Fig. 11 is within the 6 dB down region seen in Fig. 9. The directivity angle of BBSAN noise increases with frequency across all engine conditions, which is consistent with laboratory-scale overexpanded jets [43], as well as conclusions for this aircraft by Neilsen et al. [16].

2. *Mixing-Noise Trends*

The trends of the aft spatiospectral lobes across frequency and engine condition are summarized by Figs. 12 and 13. Figure 12 shows M-SONAH reconstructions in the same format as Fig. 6 but including more engine conditions, frequencies, and the lines that were traced through the multiple spatiospectral lobes. These lines are color coded to correspond with the spatiospectral lobe numbers from Fig. 3: Lobe 1 is blue, lobe 2 is green, and lobe 3 is orange. At a fixed engine condition, when frequency is increased, the lobes swing aft until they leave the aperture of the array. While that happens, new lobe(s) appear upstream and then swing aft as well. When each new lobe appears, it starts at a low amplitude, grows to a peak in the maximum radiation direction of the overall field, and then decays as it continues to swing aft and out of the aperture of the array.

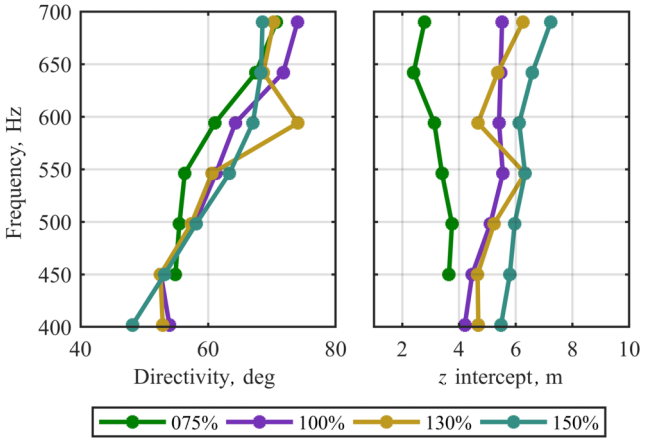

Fig. 11 Directivity and z intercept of the line traced through the BBSAN lobe for four engine conditions.

For a given frequency, lobes increase in level for higher engine conditions and their directivity angle decreases, consistent with an increasing convective Mach number of the jet. Additionally, whichever lobe originates closest to the nozzle increases in level more than the others do, thus increasing its relative contribution to the overall field. As with the discussion of Figs. 2 and 3, it appears that the increasing contribution of the forward-most lobe is the driving factor in the change of overall directivity as engine condition increases, especially in the transition from 50 to 75% ETR.

As was done for the BBSAN lobe, lines were fit to each lobe that define them by two parameters: the slope and the z intercept. The slope of the line can be expressed in terms of the jet inlet angle, giving a measure of directivity for that lobe. The z intercept of the line gives an approximation to the acoustic source region corresponding to that lobe. The directivities and z intercepts in Fig. 13 came from lines that were fitted to every spatial lobe between 60 and 400 Hz. At 60 Hz, lobe 1 (blue) begins with an aft directivity and downstream source location. As frequency increases, the directivity and z intercept tend to increase, although there appears to be some clustering of the points, suggesting that lobe 1, as identified in Fig. 3, is probably a superposition of two lobes that are not entirely separable when looking at level alone. Coherence analyses in Ref. [32] corroborate this conclusion. Lobe 2 (green) has a source region between 5 and 10 m downstream that does not change drastically with frequency but consistently shifts downstream with increasing engine condition. The directivity angle increases with increase in frequency, with as much as a 15 deg increase for 50 and 75% ETR from 150 to 400 Hz. At 130 and 150% ETR, the change in directivity across frequency is less. Lobe 3 (orange) first appears at a higher frequency than the other two lobes and has similar trends as lobe 2. Lobes 2 and 3 share similar z intercepts as the BBSAN lobe seen in Fig. 11. As engine power increases, the z intercepts for all lobes are shifted farther downstream, and the directivities shift toward the sideline. In most cases, the lines representing the several lobes stay in the same ordering relative to each other; lobe 1 remains the farthest downstream, with lobe 3 being the farthest upstream.

E. Comparison with Other Studies

The spatiospectral lobe trends discussed in this work have been partially observed by several studies in recent years. Harker et al. [44] showed one-third octave band spectra for pressures measured by a ground-based linear array parallel to the jet centerline of a tied-down high-performance military aircraft with a rectangular nozzle. Figure 2 of that paper displays the OASPL and spectra as a function of distance downstream from the nozzle, similar to Figs. 2 and 3 of this paper. At least two spatiospectral lobes are apparent at the afterburning engine condition, with the first centered at about 100 Hz and 17 m downstream of the nozzle and the second centered at 250 Hz and about

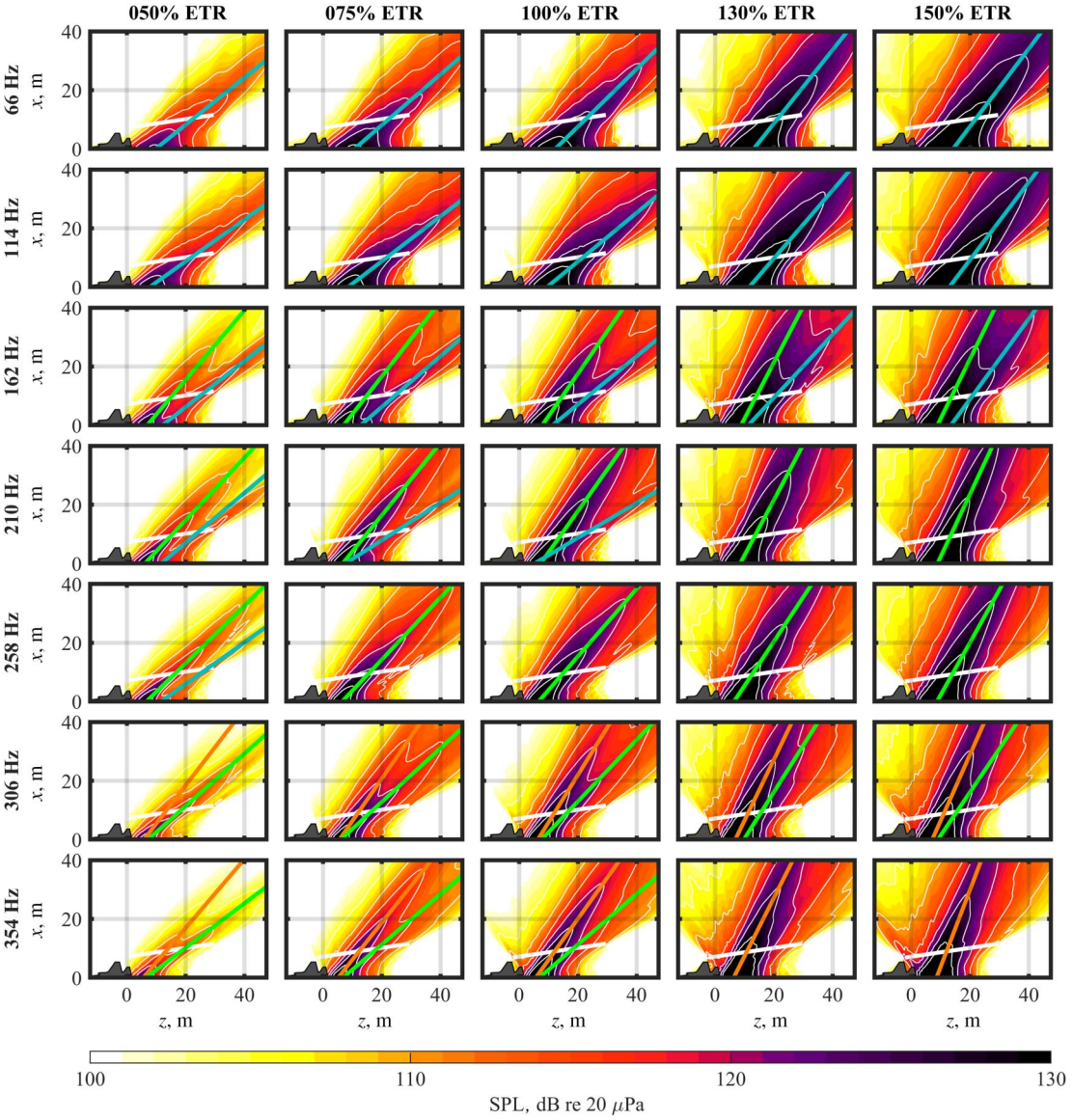

Fig. 12 M-SONAH reconstructions along the $y = 0$ plane for several frequencies and engine conditions.

10 m. Acoustic intensity vectors measured in the vicinity of that same aircraft are reported by Stout et al. [45,46]. A video attached to Ref. [45] shows a vector intensity map that changes as a function of frequency. At low frequency, the intensity vectors show a large aft directivity with apparent source region far downstream. As frequency increases, the vectors measured nearer to the nozzle grow in level relative to the far aft intensity vectors, while all vectors slightly rotate aft. This pattern is again recorded in Fig. 12 of Ref. [46], in which the angular span of the top 3 dB of intensity vectors is plotted as a function of frequency. The top 3 dB region of the radiation points far aft at low frequency, and then, as frequency increases, the angles jump upstream, shift downstream, then jump upstream again. This general pattern is the same as is observed in the columns of Fig. 12 in the current work; as frequency increases, new lobes appear upstream and grow in strength as the farther aft lobes decay and shift out of the measurement aperture.

A recent measurement of the T-7A trainer aircraft [21] with an expansive near-field array identified spatiospectral lobes in military, afterburner, and two intermediate conditions with qualitatively similar patterns across frequency and engine power as those discussed here. Similarity in the spatiospectral domains of the F-35, the T-7A, and the aircraft measured by Wall et al. [18] suggests that, with some frequency or velocity scaling, they could potentially collapse into self-similar behavior. For most military aircraft, however, flow parameters are not disclosed, thus rendering this type of analysis difficult.

Another look at the multiple lobes in the one-third octave band spectra of the same aircraft in Refs. [14,18,23,44] was performed by Tam and Parrish [22], who attempted to fit large-scale turbulent structure similarity spectra to the spectra published in Ref. [23]. Tam and Parrish [22] identified two new noise components associated to regions in the measured spectra that did not fit the ad hoc similarity spectrum they derived specifically for that study. For the first, this similarity spectrum was fit to the lower of the two peaks in the measured spectrum at an inlet angle of 115 deg, and the higher frequency component was deemed to be a new noise source (see Fig. 22 of Ref. [22]). For the second new noise source, the similarity spectrum was fit to the higher frequency peak at an inlet angle of 150 deg, and the extra low-frequency content is called a new source (see Fig. 29). These two new noise sources were then identified as fast wave indirect combustion noise and slow wave indirect combustion noise. If that aircraft under investigation has a similar spatiospectral structure as the F-35B, then it would appear that the authors are attempting to fit the similarity spectrum to lobe 2 and are calling lobe 3 fast wave indirect combustion noise and lobe 1 slow wave indirect combustion noise. Because of the high-resolution measurements provided by the current study, it is clearly seen that lobes exist across multiple engine conditions, regardless of the presence of afterburner.

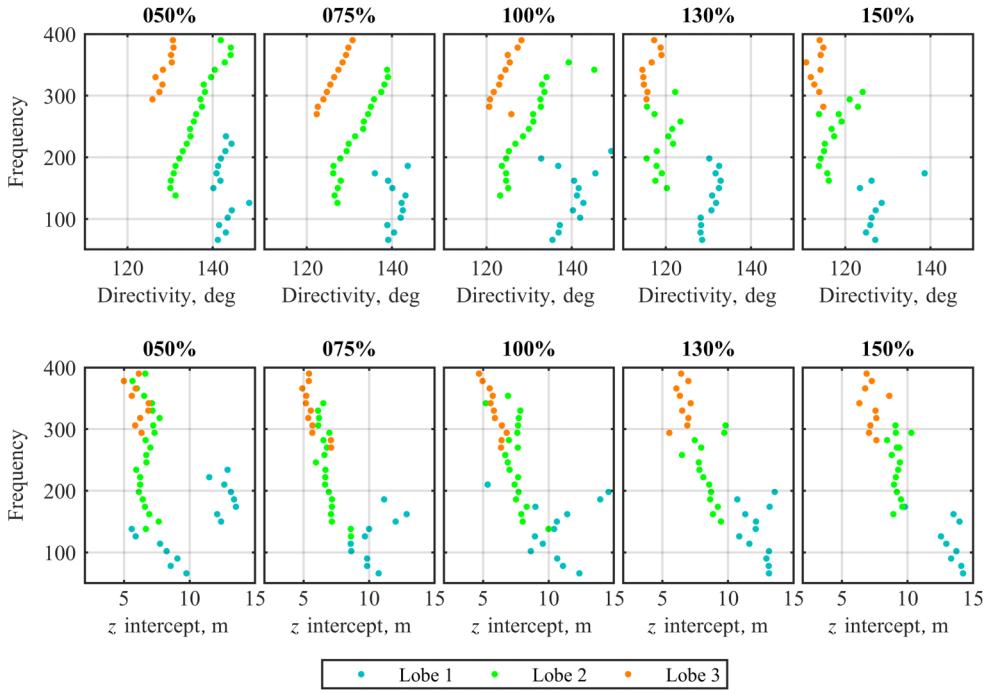

Fig. 13 Directivity angle (top row) and z intercept (bottom row) of the lines fitted through each of the spatial radiation lobes seen in the M-SONAH reconstructions.

In previous laboratory-scale investigations of jets exhausting over rigid surfaces [47–52], an additional peak in the spectrum was observed below the peak frequency of the jet noise and was attributed to the interaction of the jet with the surface. For cases in which the surface was smaller than the extent of the plume, the noise source was found to be the scattering of the jet off the edge of the surface. In cases in which the surfaces were larger than the extent of the plume and were meant to represent a rigid ground, low-frequency amplification is observed in the far aft beyond inlet angles of 150 deg [47,48]. It is noted that lobe 1 as labelled in the current work is situated below the peak frequency of the jet noise from this aircraft and is found in this far aft region. It is therefore possible that jet–ground interactions could be a contributing effect. For example, there are a few cases in Fig. 13 in which the directivity and source location of lobe 1 do not follow the same trends as the other lobes (particularly apparent at 50% ETR). It may be that, at these low frequencies, jet noise and jet–ground interaction noise are superimposed, thus corrupting the field reconstructions. Further work is needed to understand the effect of the ground on the low-frequency component of military aircraft jet noise.

In an attempt to shed light on the origin of multiple radiation lobes, Liu et al. [26] used the JENRE® large-eddy simulation (LES) solver developed at the U.S. Naval Research Laboratory to simulate a supersonic jet at a temperature of 2100 K (total temperature ratio of 7), which is comparable to operating conditions of high-performance jet engine exhaust at afterburner. Figure 21a of Ref. [26] shows a far-field spatiospectral plot, which is described as being separated into three regions: the first upstream region being dominated by BBSAN, the second region that is the region of maximum radiation, and a third, further aft region that is dominated by a lower frequency component. These three regions appear similar to those seen in Fig. 3 of this paper at afterburning engine powers, where the $z < 7$ m region is dominated by BBSAN, 7 m $< z <$ 15 m is dominated by lobes 2–5, and $z >$ 15 m downstream is dominated by the low-frequency lobe 1. Leete et al. [29] investigated the coherence of the LES-generated field of Ref. [26] and found that the BBSAN component originated from the potential core region where shock cells are present, the region of maximum radiation originated from the supersonic portion of the jet, and the far aft radiation originated from an extended region around the end of the supersonic core. The source localizations of the BBSAN in Fig. 11 and the lobes in the afterburner cases in Fig. 13 agree qualitatively with the pattern found in the LES data set, with BBSAN originating in feasible locations for shock cells and lobe 1 appearing farther downstream than lobes 2 and 3.

An important distinction between the LES of the highly heated laboratory-scale jet [26] and F-35 data seen in the present work is that the LES does not contain multiple spectral peaks, simply a smooth transition from spectra with a high-frequency peak toward the sideline to a low-frequency peak in the far aft. The only time any discrete spatiospectral content is seen in the LES is when the coherence with the field is calculated to a reference point along the nozzle lipline where shock cells are present (see Fig. 7 of Ref. [29]). The coherence of the field appears to split into spatiospectral lobe-type patterns, suggesting that shock cells contribute to the presence of distinct lobes. However, without more knowledge of the plume characteristics of the F-35, more specific comparisons cannot be made.

V. Conclusions

The sound field in the vicinity of a tied-down F-35B aircraft is examined for engine powers ranging from 25 to 150% ETR. The OASPL across a linear ground array approximately parallel to the shear layer show that as engine power increases, the directivity of the field in the main radiation direction shifts toward the sideline. Spatiospectral maps along the array show that trends in the jet noise field can be described as a superposition of multiple spatiospectral lobes, and the trends in overall level with engine power are explained by the number of lobes present and their distribution of amplitudes.

M-SONAH reconstructions of the field in the vicinity of the aircraft allow for a detailed look at the evolution of each spatiospectral lobe across frequency and engine power. At a single engine condition with increasing frequency, the lobes swing farther aft until they pass beyond the downstream extent of the array. While that happens, new lobe(s) appear upstream and then swing aft as well. As engine power increases for a fixed frequency, all lobes increase in level, and their directivity shifts slightly toward the sideline. Additionally, whichever lobe is the farthest upstream increases in level more than the other lobes present at that frequency, which seems to be the largest contributor to the overall directivity shifting forward.

The extra detail provided by this measurement of the F-35B along with the M-SONAH reconstructions of the field sheds light on previous measurements of similar high-performance military aircraft. These and prior data show that looking at the main radiation region

from high-performance military jet aircraft as a single phenomenon is insufficient. The paradigm needs to shift to thinking of the main radiation lobe as a superposition of multiple, overlapping lobes, the trends of which across frequency and engine power dictate the trends of the overall field. The source mechanisms involved in producing the multiple radiation lobes are still unknown, although their presence at low engine powers suggests they are not combustion related. Also unknown is why these phenomena appear to be more prominent in the current measurement of the F-35B than measurements of other aircraft, laboratory-scale jets, and numerical simulations. Answering these questions is necessary to have a complete understanding of aeroacoustic noise from full-scale high-performance jet aircraft.

Acknowledgments

The authors gratefully acknowledge funding for the measurements provided through the F-35 Joint Program Office and U.S. Air Force Research Laboratory. K. M. Leete was funded by an appointment to the Student Research Participation Program at the U.S. Air Force Research Laboratory (USAFRL), 711th Human Performance Wing, Human Effectiveness Directorate, Warfighter Interface Division, Battlespace Acoustics Branch administered by the Oak Ridge Institute for Science and Education through an interagency agreement between the U.S. Department of Energy and USAFRL. Distribution A: Approved for public release, distribution unlimited. F-35 PAO Cleared 07/21/2020, JSF20-612.

References

[1] Dougherty, R. P., "Improved Generalized Inverse Beamforming for Jet Noise," *International Journal of Aeroacoustics*, Vol. 11, Nos. 3–4, 2012, pp. 259–289. https://doi.org/10.1260/1475-472X.11.3-4.259

[2] Papamoschou, D., Morata, D., and Shah, P., "Inverse Acoustic Methodology for Continuous-Scan Phased Arrays," *AIAA Journal*, Vol. 57, No. 12, 2019, pp. 5126–5141. https://doi.org/10.2514/1.J058085

[3] Podboy, G. G., Bridges, J. E., and Henderson, B. S., "Phased Array Noise Source Localization Measurements of an F404 Nozzle Plume at Both Full and Model Scale," *Proceedings of the ASME Turbo Expo 2010: Power for Land, Sea, and Air*, Vol. 1, ASME, New York, June 2010, pp. 179–208. https://doi.org/10.1115/GT2010-22601

[4] Schlinker, R., Liljenberg, S., Polak, D., Post, K., Chipman, C., and Stern, A., "Supersonic Jet Noise Characteristics & Propagation: Engine and Model Scale," AIAA Paper 2007-3623, 2007. https://doi.org/10.2514/6.2007-3623

[5] Brusniak, L., Underbrink, J., Nesbitt, E., Lynch, D., and Martinez, M., "Phased Array Measurements of Full-Scale Engine Exhaust Noise," AIAA Paper 2007-3612, 2007. https://doi.org/10.2514/6.2007-3612

[6] Harker, B. M., Gee, K. L., Neilsen, T. B., Wall, A. T., and James, M. M., "Source Characterization of Full-Scale Tactical Jet Noise from Phased-Array Measurements," *Journal of the Acoustical Society of America*, Vol. 146, No. 1, 2019, pp. 665–680. https://doi.org/10.1121/1.5118239

[7] Maynard, J. D., Williams, E. G., and Lee, Y., "Nearfield Acoustical Holography: I. Theory of Generalized Holography and the Development of NAH," *Journal of the Acoustical Society of America*, Vol. 78, No. 4, 1985, pp. 1395–1413. https://doi.org/10.1121/1.392911

[8] Hald, J., "Basic Theory and Properties of Statistically Optimized Near-Field Acoustical Holography," *Journal of the Acoustical Society of America*, Vol. 125, No. 4, 2009, pp. 2105–2120. https://doi.org/10.1121/1.3079773

[9] Lee, M., and Bolton, J., "Source Characterization of a Subsonic Jet by Using Near-Field Acoustical Holography," *Journal of the Acoustical Society of America*, Vol. 121, No. 2, 2007, pp. 967–977. https://doi.org/10.1121/1.2404626

[10] Long, D., "Jet Noise Source Location via Acoustic Holography and Shadowgraph Imagery," AIAA Paper 2008-2888, 2008. https://doi.org/10.2514/6.2008-2888

[11] Shah, P., Vold, H., and Yang, M., "Reconstruction of Far-Field Noise Using Multireference Acoustical Holography Measurements of High-Speed Jets," AIAA Paper 2011-2772, 2011. https://doi.org/10.2514/6.2011-2772

[12] Shah, P. N., Vold, H., Hensley, D., Envia, E., and Stephens, D., "A High-Resolution Continuous-Scan Acoustic Measurement Method for Turbofan Engine Applications," *Journal of Turbomachinery*, Vol. 137, No. 12, 2015, Paper 121002. https://doi.org/10.1115/1.4031341

[13] Wall, A. T., Gee, K. L., and Neilsen, T. B., "Multisource Statistically Optimized Near-Field Acoustical Holography," *Journal of the Acoustical Society of America*, Vol. 137, No. 2, 2015, pp. 963–975. https://doi.org/10.1121/1.4906585

[14] Wall, A. T., Gee, K. L., Neilsen, T. B., McKinley, R. L., and James, M. M., "Military Jet Noise Source Imaging Using Multisource Statistically Optimized Near-Field Acoustical Holography," *Journal of the Acoustical Society of America*, Vol. 139, No. 4, 2016, pp. 1938–1950. https://doi.org/10.1121/1.4945719

[15] Wall, A. T., Leete, K. M., Gee, K. L., Neilsen, T. B., James, M. M., and McKinley, R. L., "Preliminary Investigation of Multilobe Fighter Jet Noise Sources Using Acoustical Holography," AIAA Paper 2017-3520, 2017. https://doi.org/10.2514/6.2017-3520

[16] Neilsen, T. B., Vaughn, A. B., Gee, K. L., Swift, S. H., Wall, A. T., Downing, J. M., and James, M. M., "Three-Way Spectral Decompositions of High-Performance Military Aircraft Noise," *AIAA Journal*, Vol. 57, No. 8, 2019, pp. 3467–3479. https://doi.org/10.2514/1.J057992

[17] Vaughn, A. B., Neilsen, T. B., Gee, K. L., Wall, A. T., Micah Downing, J., and James, M. M., "Broadband Shock-Associated Noise from a High-Performance Military Aircraft," *Journal of the Acoustical Society of America*, Vol. 144, No. 3, 2018, pp. EL242–EL247. https://doi.org/10.1121/1.5067445

[18] Wall, A. T., Gee, K. L., James, M. M., Bradley, K. A., McInerny, S. A., and Neilsen, T. B., "Near-Field Noise Measurements of a High Performance Military Jet Aircraft," *Noise Control Engineering Journal*, Vol. 60, No. 4, 2012, pp. 421–434. https://doi.org/10.3397/1.3701021

[19] James, M. M., Salton, A. R., Downing, J. M., Gee, K. L., Neilsen, T. B., Reichman, B. O., McKinley, R., Wall, A. T., and Gallagher, H., "Acoustic Emissions from F-35 Aircraft During Ground Run-Up," AIAA Paper 2015-2375, 2015. https://doi.org/10.2514/6.2015-2375

[20] Tam, C. K., Aubert, A. C., Spyropoulos, J. T., and Powers, R. W., "On the Dominant Noise Components of Tactical Aircraft: Laboratory to Full Scale," *Journal of Sound and Vibration*, Vol. 422, May 2018, pp. 92–111. https://doi.org/10.1016/j.jsv.2018.02.023

[21] Leete, K. M., Vaughn, A. B., Bassett, M. S., Rasband, R. D., Novakovich, D. J., Gee, K. L., Campbell, S. C., Mobley, F. S., and Wall, A. T., "Jet Noise Measurements of an Installed GE F404 Engine," AIAA Paper 2021-1638, 2021. https://doi.org/10.2514/6.2021-1638

[22] Tam, C. K. W., and Parrish, S. A., "Noise of High-Performance Aircraft at Afterburner," *Journal of Sound and Vibration*, Vol. 352, Sept. 2015, pp. 103–128. https://doi.org/10.1016/j.jsv.2015.04.010

[23] Neilsen, T. B., Gee, K. L., Wall, A. T., and James, M. M., "Similarity Spectra Analysis of High-Performance Jet Aircraft Noise," *Journal of the Acoustical Society of America*, Vol. 133, No. 4, 2013, pp. 2116–2125. https://doi.org/10.1121/1.4792360

[24] Liu, J., Corrigan, A. T., Kailasanath, K., Heeb, N. S., and Gutmark, E. J., "Numerical Study of Noise Sources Characteristics in an Underexpanded Jet Flow," AIAA Paper 2024-2604, 2014. https://doi.org/10.2514/6.2014-2604

[25] Liu, J., Corrigan, A. T., Kailasanath, K., and Gutmark, E. J., "Impact of Chevrons on Noise Source Characteristics in Imperfectly Expanded Jet Flows," AIAA Paper 2015-2835, 2015. https://doi.org/10.2514/6.2015-2835

[26] Liu, J., Corrigan, A. T., Kailasanath, K., and Taylor, B. D., "Impact of the Specific Heat Ratio on the Noise Generation in a High-Temperature Supersonic Jet," AIAA Paper 2016-2125, 2016. https://doi.org/10.2514/6.2016-2125

[27] Liu, J., Kailasanath, K., and Gutmark, E. J., "Similarity Spectra Analysis in Highly Heated Supersonic Jets Using Large-Eddy Simulations," AIAA Paper 2017-0926, 2017. https://doi.org/10.2514/6.2017-0926

[28] Schmidt, O. T., Towne, A., Rigas, G., Colonius, T., and Brès, G. A., "Spectral Analysis of Jet Turbulence," *Journal of Fluid Mechanics*, Vol. 855, Sept. 2018, pp. 953–982. https://doi.org/10.1017/jfm.2018.675

[29] Leete, K. M., Gee, K. L., Liu, J., and Wall, A. T., "Coherence Analysis of the Noise from a Simulated Highly Heated Laboratory-Scale Jet," *AIAA Journal*, Vol. 58, No. 8, 2020, pp. 3426–3435. https://doi.org/10.2514/1.J059112

[30] Wall, A. T., Gee, K. L., Leete, K. M., Neilsen, T. B., Stout, T. A., and James, M. M., "Partial-Field Decomposition Analysis of Full-Scale Supersonic Jet Noise Using Optimized-Location Virtual References," *Journal of the Acoustical Society of America*, Vol. 144, No. 3, 2018, pp. 1356–1367. https://doi.org/10.1121/1.5053580

[31] Harker, B. M., Gee, K. L., Neilsen, T. B., Wall, A. T., and James, M. M., "Beamforming-Based Wavepacket Model for Noise Environment Predictions of Tactical Aircraft," AIAA Paper 2017-4048, 2017. https://doi.org/10.2514/6.2017-4048

[32] Swift, S. H., Gee, K. L., Neilsen, T. B., Wall, A. T., Downing, J. M., and James, M. M., "Spatiotemporal-Correlation Analysis of Jet Noise from a Round Nozzle High-Performance Aircraft," AIAA Paper 2018-3938, 2018. https://doi.org/10.2514/6.2018-3938

[33] Steiner, R., and Hald, J., "Near-Field Acoustical Holography Without the Errors and Limitations Caused by the Use of Spatial DFT," *International Journal of Acoustics and Vibration*, Vol. 6, No. 2, 2001, pp. 83–89. https://doi.org/10.20855/ijav.2001.6.278

[34] Hald, J., "STSF—A Unique Technique for scan-Based Near-Field Acoustic Holography Without Restrictions on Coherence," *Brüel & Kjær Technical Review No. 1*, 1989, https://www.bksv.com/media/doc/bv0035.pdf.

[35] Wall, A. T., Gee, K. L., Krueger, D. W., Neilsen, T. B., Sommerfeldt, S. D., and James, M. M., "Aperture Extension for Near-Field Acoustical Holography of Jet Noise," *Proceedings of Meetings on Acoustics*, Vol. 14, No. 1, 2013, Paper 065001. https://doi.org/10.1121/1.4794833

[36] Cho, Y. T., Bolton, J. S., and Hald, J., "Source Visualization by Using Statistically Optimized Near-Field Acoustical Holography in Cylindrical Coordinates," *Journal of the Acoustical Society of America*, Vol. 118, No. 4, 2005, pp. 2355–2364. https://doi.org/10.1121/1.2036252

[37] Williams, E. G., "Regularization Methods for Near-Field Acoustical Holography," *Journal of the Acoustical Society of America*, Vol. 110, No. 4, 2001, pp. 1976–1988. https://doi.org/10.1121/1.1404381

[38] Leete, K. M., Wall, A. T., Gee, K. L., Neilsen, T. B., Downing, J. M., and James, M. M., "Numerical Validation of Using Multisource Statistically-Optimized Near-Field Acoustical Holography in the Vicinity of a High-Performance Military Aircraft," *Proceedings of Meetings on Acoustics*, Vol. 31, No. 1, 2017, Paper 040007. https://doi.org/10.1121/2.0000895

[39] Suzuki, T., "A Review of Diagnostic Studies on Jet-Noise Sources and Generation Mechanisms of Subsonically Convecting Jets," *Fluid Dynamics Research*, Vol. 42, No. 1, 2010, Paper 014001. https://doi.org/10.1088/0169-5983/42/1/014001

[40] Laufer, J., Schlinker, R. H., and Kaplan, R. E., "Experiments on Supersonic Jet Noise," *AIAA Journal*, Vol. 14, 1976, pp. 489–497. https://doi.org/10.2514/3.61388

[41] Hileman, J. I., Thurow, B. S., Caraballo, E. J., and Samimy, M., "Large-Scale Structure Evolution and Sound Emission in High-Speed Jets: Real-Time Visualization with Simultaneous Acoustic Measurements," *Journal of Fluid Mechanics*, Vol. 544, Dec. 2005, pp. 277–307. https://doi.org/10.1017/S002211200500666X

[42] Murray, N. E., and Baars, W. J., "Passive Nozzle-Based Technology for the Reduction of Heated Supersonic Jet Noise," AIAA Paper 2019-2729, 2019. https://doi.org/10.2514/6.2019-2729

[43] Tanna, H. K., "An Experimental Study of Jet Noise Part II: Shock Associated Noise," *Journal of Sound and Vibration*, Vol. 50, No. 3, 1977, pp. 429–444. https://doi.org/10.1016/0022-460X(77)90494-1

[44] Harker, B. M., Neilsen, T. B., Gee, K. L., Wall, A. T., and James, M. M., "Spatiotemporal-Correlation Analysis of Jet Noise from a High-Performance Military Aircraft," *AIAA Journal*, Vol. 54, No. 5, 2016, pp. 1554–1566. https://doi.org/10.2514/1.J054442

[45] Stout, T. A., Gee, K. L., Neilsen, T. B., Wall, A. T., and James, M. M., "Acoustic Intensity near a High-Powered Military Jet Aircraft," *Journal of the Acoustical Society of America*, Vol. 138, No. 1, 2015, pp. EL1–EL7. https://doi.org/10.1121/1.4921746

[46] Stout, T. A., Gee, K. L., Neilsen, T. B., Wall, A. T., and James, M. M., "Source Characterization of Full-Scale Jet Noise Using Acoustic Intensity," *Noise Control Engineering Journal*, Vol. 63, No. 6, 2015, pp. 522–536. https://doi.org/10.3397/1/376346

[47] Powers, R. W., McLaughlin, D. K., and Morris, P. J., "Noise Reduction in Supersonic Jets Exhausting over a Simulated Aircraft Carrier Deck," *Journal of Aircraft*, Vol. 55, No. 1, 2018, pp. 310–324. https://doi.org/10.2514/1.C034213

[48] Worden, T. J., Shih, C., and Alvi, F. S., "Supersonic Jet Impingement on a Model-Scale Jet Blast Deflector," *AIAA Journal*, Vol. 55, No. 8, 2017, pp. 2522–2536. https://doi.org/10.2514/1.J055664

[49] von Glahn, U. H., Goodykoontz, J. H., and Wagner, J. M., "Nozzle Geometry and Forward Velocity Effects on Noise for CTOL Engine-over-the-Wing Concept," Jan. 1973, https://ntrs.nasa.gov/search.jsp?R=19730025009.

[50] Podboy, G. G., "Jet-Surface Interaction Test: Phased Array Noise Source Localization Results," *Proceedings of the ASME Turbo Expo 2012: Turbine Technical Conference and Exposition*, Vol. 1, Copenhagen, Denmark, June 2012, pp. 381–414. https://doi.org/10.1115/GT2012-69801

[51] Brown, C. A., "Jet-Surface Interaction Test: Far-Field Noise Results," *Journal of Engineering for Gas Turbines and Power*, Vol. 135, No. 7, 2013, Paper 071201. https://doi.org/10.1115/1.4023605

[52] Rego, L., Casalino, D., Avallone, F., and Ragni, D., "Noise Amplification Effects due to Jet-Surface Interaction," AIAA Paper 2019-0001, 2019.

D. Papamoschou
Associate Editor